Materials Horizons

ROYAL SOCIETY OF CHEMISTRY

COMMUNICATION

View Article Online
View Journal | View Issue

Cite this: *Mater. Horiz.*, 2025, **12**, 1179

Received 30th September 2024,
Accepted 14th November 2024

DOI: 10.1039/d4mh01360c

rsc.li/materials-horizons

Studies of the mechanically induced reactivity of graphene with water using a 2D-materials strain reactor†

Nathaniel Hawthorne,[a] Edward J. Broker Jr,[a] Yutian Bao,[c] Sayan Banerjee,[c] Quentarius Moore,[a] Camille Cardinal,[ad] Jimmy Ha,[a] Ulisses D. Braga,[ae] Andrew M. Rappe[c] and James D. Batteas*[ab]

Using mechanical force to induce chemical reactions with two-dimensional (2D) materials provides an approach for both understanding mechanochemical processes on the molecular level, and a potential method for using mechanical strain as a means of directing the functionalization of 2D materials. To investigate this, we have designed a modular experimental platform which allows for *in situ* monitoring of reactions on strained graphene *via* Raman spectroscopy as a function of time. Both the strain present in graphene and the corresponding chemical changes it undergoes in the presence of a reagent can be followed concomitantly. As a case study, we have experimentally monitored and theoretically modeled the reactivity of a suspended single-layer graphene membrane under strain with water, where the graphene is strained *via* an applied backing pressure. While exposure of the unstrained membrane to water does not drive a chemical reaction, distortion of the membrane causes a rise in the I_D/I_G peak ratio, indicating an initial lattice conversion from crystalline to nanocrystalline due to reaction with water. With continued reaction, a decrease in the I_D/I_G peak ratio is then seen, indicative of a nanocrystalline to amorphous lattice transition. Using density functional theory (DFT) calculations, the reaction of water on graphene has been determined to be nucleated by epoxide defects, with the reaction barrier decreasing by nearly 5× for the strained *vs.* unstrained graphene. While demonstrated here for graphene, this approach also provides the opportunity to examine a host of force-driven chemical reactions with 2D materials.

New concepts

Here, through paired experimental and computational studies, we demonstrate graphene's penchant for undergoing chemical reactions under applied mechanical strains. While considerable work has explored the chemical reactivity of 2D materials in general to tune their properties, we pursue the ways in which the reactivity of isolated 2D materials can be controlled by applied mechanical distortions. Here, a newly designed 2D materials strain reactor was employed, allowing us to pair *in situ* spectroscopies and microscopies, to provide time resolved characterization of strained single-layer graphene as it reacts with water under applied force. The striking spectral changes of graphene observed experimentally, and the chemical changes that occur as reaction proceeds, are further revealed by density functional theory calculations of the reaction energy landscapes of graphene under distortion, and illustrate the importance of defects in initiating such mechanically driven reactions. These studies afford a solid foundation for future work aimed at using directed mechanical forces to precisely chemically pattern graphene and other 2D materials. The increased understanding of mechanochemical methods for directed functionalization of 2D materials, expands our toolset for controlling the robust optoelectronic properties of such materials, proffering new directions for meeting the material needs of ever-advancing technologies.

1. Introduction

Utilizing mechanical force to induce chemical reactions has gained significant interest as a route to synthesize desired products with better yields and selectivity than traditional solvent-based processes.[1–3] In addition to expanding the field of green chemistry, the use of mechanochemistry is also potentially viable for a range of applications, such as the development of touch-based electronics (mechanotransduction),[4,5] friction control (tribochemistry),[6–8] and food processing.[9–11]

However, while the principles of mechanochemistry are better understood at the atomistic level, most macroscale applications of mechanochemistry suffer from ambiguity in the understanding of their processes.[2,12,13] There have been recent advances to quantify the directionality and magnitude of

[a] *Department of Chemistry, Texas A&M University, College Station, TX 77843, USA. E-mail: batteas@chem.tamu.edu*
[b] *Department of Materials Science and Engineering, Texas A&M University, College Station, TX 77843, USA*
[c] *Department of Chemistry, University of Pennsylvania, Philadelphia, PA 19104, USA*
[d] *School of Polymer Science and Engineering, University of Southern Mississippi, Hattiesburg, MS 39401, USA*
[e] *Department of Chemistry, University of Texas at Austin, Austin, TX 87812, USA*

† Electronic supplementary information (ESI) available. See DOI: https://doi.org/10.1039/d4mh01360c

the forces involved in macroscale reactors (*i.e.*, ball mills[14]) though there remains much work to be done to connect the role of mechanical forces at the atomistic and macroscopic length scales for driving reactions. Toward this goal, we have recently developed a reactor system capable of applying force (measured as strain) in a directed manner to two-dimensional material membranes while monitoring changes to their spectral and morphological properties *in situ* in response to the applied forces.

Two-dimensional (2D) materials, such as graphene, serve as a unique platform for studying the influence that force can have on reactivity. Their well-defined structural and spectral properties provide a distinct baseline for monitoring changes under applied force, while their lack of dangling bonds keeps their basal planes generally unreactive under ambient conditions.[15,16] When distorted out-of-plane, however, 2D materials become susceptible to increased reactivity. We and others have shown this for an aryl radical addition reactions with graphene,[17,18] with similar results for other chemical systems.[19–21] In addition to local distortions driving reaction, we have also seen that introducing curvature drives the direction of molecular motion (*i.e.* diffusion) on graphene.[17,22–24] The increased reactivity with out-of-plane distortion stems from a decrease in the electron delocalization across the sp^2 lattice as the angle between the adjacent p_z orbitals changes, leading to rearrangements in the p_z charge density.

While the experimental studies cited above used the substrate to introduce strain to the graphene, here a reactor system was designed and tested to allow for strain to be introduced and for its corresponding impact on the reactivity of graphene to be followed spectroscopically *in situ*. Termed the 2D-materials strain reactor (2D-MSR), this system allows for real time characterization of graphene membranes suspended on pores on TEM grids, in both the presence and absence of a backing pressure. By attaching these membranes to specially designed caps mounted on the reactor base, the membranes are brought into contact with a backing pressure of gas or liquid that is flowing through the system. The 2D-MSR was designed to be compatible with an existing confocal Raman/atomic force microscope, such that membranes are directly aligned with the objective to monitor spectroscopic properties as the tailorable force is applied (Fig. 1). For graphene, through comparisons of the D and G peak intensities and the G and 2D peak positions, information regarding reactivity and strain, respectively, could be readily attained.

Herein, we describe the use of the 2D-MSR to examine the strain-driven reactivity of graphene with water as a model system to explore the influence that mechanical distortions have on the reactivity of 2D materials. Both reactivity and strain can be directly monitored in graphene through Raman spectroscopy, as its Raman peaks are well defined and attributable to distinct characteristics of the lattice. Most pertinent to this mechanically induced reaction are the D, G, and 2D peaks which arise at or around 1350, 1580, and 2700 cm^{-1}, respectively. The G peak is observed in all graphitic systems and is attributed to the doubly degenerate E_{2g} mode.[25] The D peak arises from lattice defects,[25] and its intensity is directly proportional to the extent of disorder.[26] The 2D peak is an overtone of the D peak; because the 2D peak originates from a process where momentum conservation is satisfied by two phonons with opposite wave vectors, no defects are required for excitation, and are thus always present. From Raman spectroscopy measurements, we have seen that freely suspended (unstrained) graphene does not react upon exposure to water. However, upon the application of a backing pressure, the membrane is distorted and the graphene becomes more susceptible to reaction, as evidenced by an increase in the I_D/I_G peak ratio. Interestingly, as the reaction proceeds, the I_D/I_G ratio eventually begins to decrease, indicating that as the reaction with water continues, the graphene then undergoes a transition from a crystalline to a nanocrystalline surface, and then ultimately to a predominantly disordered, amorphous lattice.

To better understand the strain-driven reaction of water with graphene, density functional theory (DFT) has been employed both to reveal the chemical processes occurring on the graphene surface and to understand the corresponding changes in the I_D/I_G ratio during reaction. It has been shown that graphene has strong chemical resistance and high thermal stability, though its catalytic properties can be greatly improved with doping or defects.[27–29] Thus, the effect of defects is also investigated to better represent the realistic experimental environment. As described below, the presence of defects (such as epoxides) is needed to nucleate the dissociation of water on graphene, and that under applied strain, the reaction barrier decreases by nearly 5×, resulting in the addition of –H and –OH

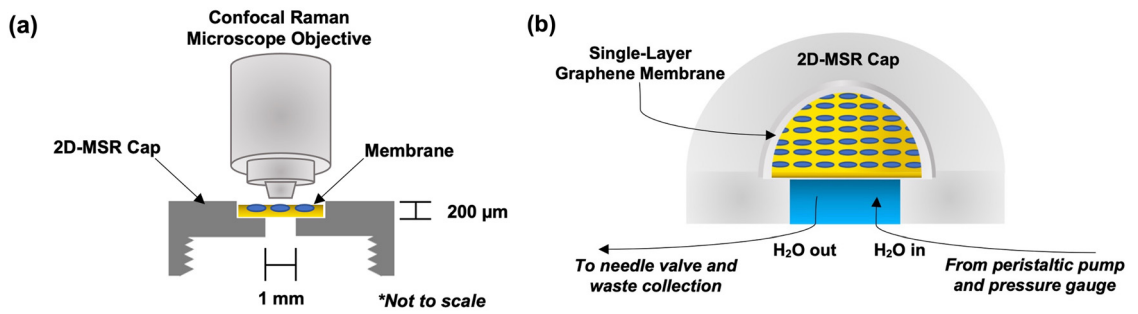

Fig. 1 Overview of the 2D-materials strain reactor (2D-MSR). Schematic of (a) the confocal microscope objective and 2D-MSR cap and (b) the 2D-MSR cap to which the graphene membrane is affixed.

species to the graphene surface. Based on the calculations of preferred adsorption sites on curved graphene, we can further comprehend the disordering and potential structural transformation of graphene under pressure.

2. Results and discussion

2.1 The 2D-materials strain reactor (2D-MSR)

The reactor system was designed and produced in-house as a way to monitor *in situ* reactivity of 2D materials, inspired by prior work in the literature.[30,31] Its design specifications can be found in the experimental section. To illustrate the functioning of the system regarding these experiments, the basic layout of the 2D-MSR is shown in Fig. 1. With the 2D-MSR, 2D membranes can be optically imaged and spectroscopically characterized with or without an applied force supplied by some liquid or gas. For this study, neutral nanopure water was used as a backing pressure medium to monitor the reactivity of graphene when distorted out-of-plane. While curvature is induced by the backing pressure supplied by the 2D-MSR, turning off the peristaltic pump or removing the sample cap will result in the suspended graphene returning to its previous unstrained state. There was no detected degradation of graphene observed as a result of the applied pressure.

2.2 Reaction of water with free-standing unstrained graphene

As a reference, a membrane sample adhered to a 2D-MSR cap underwent a time-dependent series of spectral measurements to determine that exposure to water without applied pressure would not lead to a change in reactivity. Initial spectra were taken of four pores before the sample was exposed to nanopure water for 10 min. After drying, spectra were taken of the same four pores, and this process was then repeated up to a 70 min cumulative exposure time.

The experimental setup is displayed in Fig. 2a. By having the sample inverted and the back of the cap filled with the nanopure water, the side of the membrane that would be in contact with water during pressurized experiments will also be in contact for these reference experiments. The membrane seal could be leak-checked by observing if any water had pooled under the sample. No leaks were observed during the measurements, and the membrane was optically identical before and after the exposure test.

As can be seen, there was little change in the I_D/I_G ratio for the observed membranes before exposure to water and after the longest exposure time. The time-resolved spectra for a representative suspended region are shown in Fig. 2c. The spectra are offset for clarity and normalized to the height of the I_G peak. Beyond the initial small increase in the D-band, the consistent I_D/I_G ratio is indicative of no reaction, as a reaction would lead to increased disorder of the lattice with sp^2 to sp^3 conversion, and a resulting growth of the D peak.

An optical image with each of four monitored pores marked is shown in Fig. 3a. Additionally, the corresponding I_D/I_G ratios for each region as a function of exposure time are displayed in Fig. 3b. The average I_D/I_G ratio and standard deviation of the four suspended pores for each exposure time are indicated in Fig. 3b by black diamonds. The average I_D/I_G ratio for each exposure time is the same within error, ranging from 0.2 ± 0.1 for $t = 0$ min, to 0.20 ± 0.07 for $t = 70$ min.

The calculated strain for each monitored region as a function of exposure time (relative to 0% for the membrane in air), is displayed in Fig. 3c and was calculated based on eqn (1):

$$\varepsilon = 0.02\left(\omega_G - \omega_G^\circ\right) - 0.028\left(\omega_{2D} - \omega_{2D}^\circ\right), \quad (1)$$

as has been previously established in the literature,[32,33] where ω_G and ω_{2D} are the G and 2D peak positions for each measurement, and ω_G° and ω_{2D}° are the G and 2D peak positions of the membrane in air at $t = 0$ min. Values are positive for expanded area and negative for contracted area. Here, little strain is introduced to the lattice when exposed to water under ambient

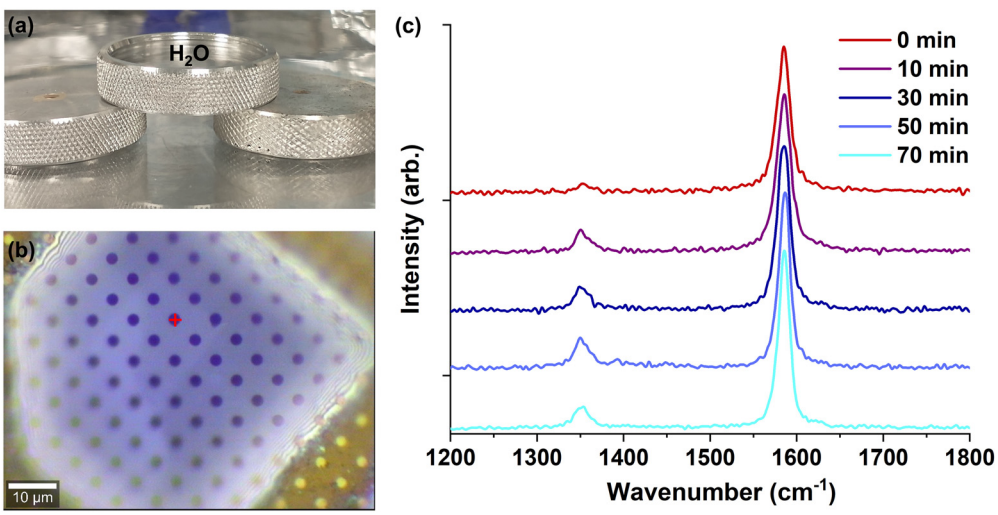

Fig. 2 Optical images and spectra for exposure test. (a) Cap filled with nanopure water for prolonged water-membrane contact. (b) Array of suspended graphene regions before exposure to water, which appeared optically unchanged after the length of the experiment. (c) Normalized Raman spectra taken at regular intervals corresponding to the red cross in (b), offset for clarity.

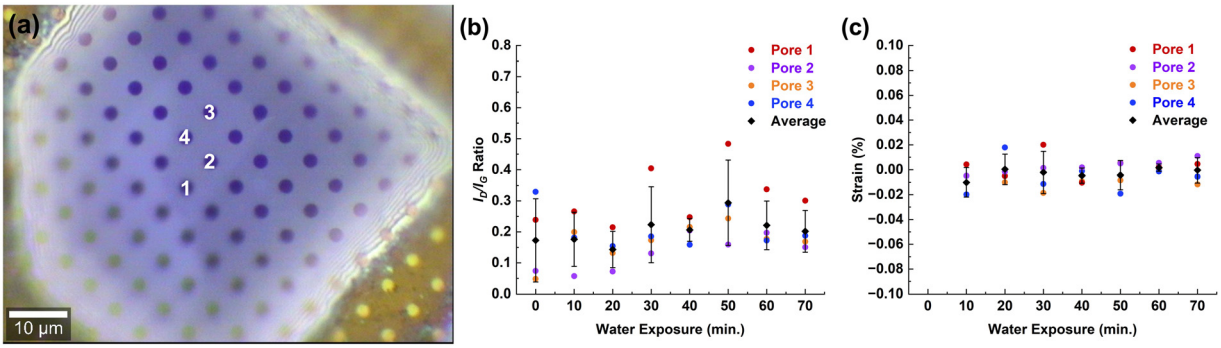

Fig. 3 Reactivity of suspended graphene after exposure test. (a) Optical image corresponding to each pore monitored in (b) and (c). (b) Change in I_D/I_G ratio as a function of exposure time. (c) Change in lattice strain as a function of exposure time. The black diamonds and error bars in (b) and (c) correspond to the average value and standard deviation of the four monitored pores at every time point. Those bars ($\pm 1\sigma$) not readily seen are obfuscated by the individual data points.

pressure, with the average values ranging from $-0.01 \pm 0.01\%$ to $0.002 \pm 0.003\%$, but all are centred around 0%. From Fig. 2 and 3, simple exposure to nanopure water in the absence of applied force was insufficient to drive reaction with water.

2.3 Reaction of water with graphene under strain

To determine if an applied strain could drive a reaction, a fresh graphene membrane was mounted in the 2D-MSR. Raman measurements were made as a function of continued exposure time when a backing pressure was applied. The backing pressure, monitored by a pressure gauge located between the peristaltic pump and the 2D-MSR inlet, was maintained between 0.14 and 0.76 kPa over the course of the experiment. The needle valve's position was held constant to avoid intentionally changing the backing pressure. Initial spectral measurements were not taken for the first $\approx$ 20 min, during which time the membrane was observed optically to confirm a lack of leaks. Afterward, measurements were taken approximately every 3 min.

Slight fluctuations in pressure occurred due to rotation of the peristaltic pump rollers, which led to a variation in spectral intensity due to the membrane moving in and out of the confocal plane. Fig. 4 illustrates the integrated spectral area of the graphene 2D peak (2650–2750 cm^{-1}) every 0.5 s for a 40 s time frame. These pump rotation speed dependent maxima and minima in the spectral intensity occurred with a periodicity of $\approx$10 s. At the maxima, the Lorentz fit of the 2D peak area is $\approx$3.4$\times$ that at its minima. For this reason, all spectra were collected as an average of 20 cumulative spectra over a 1 min period, and as such, are representative of the average strain on the membrane over that time frame.

Unlike the unstrained case shown above, when examining the reaction of water with graphene under strain, the D peak is seen to initially increase as a function of reaction time (Fig. 5a) from t = 21.5 to t = 51.5 min. The increasing D-peak is indicative of increasing disorder in graphene as the lattice was undergoing local sp^2 to sp^3 conversion at binding sites upon the formation of out-of-plane covalent bonds, presumably with water or its dissociated components (–H and –OH).

From t = 51.5 to t = 63.5 min, little change is observed. However, unexpectedly, the D-peak starts to decrease at

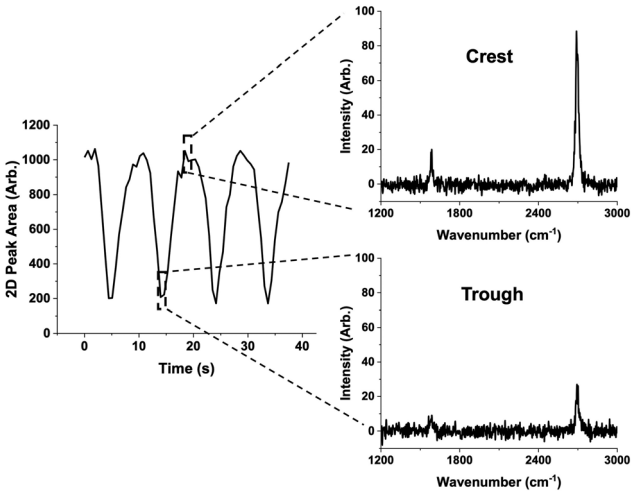

Fig. 4 Variation in 2D peak signal intensity. Integrated intensity between 2650 cm^{-1} and 2750 cm^{-1} as a function of time for a continuous series of spectra, each with a 0.5 s integration time. Top right is the background subtracted average spectra for t = 18–19.5 s, illustrating maximum spectral intensity. Bottom right is the background subtracted average spectra for t = 13–14.5 s, illustrating minimum spectral intensity.

t = 63.5 min (Fig. 5b). The same trend of increase, inflection point, and decrease was seen for the D′ peak, as well. The D′ peak at $\approx$ 1620 cm^{-1} rises and declines in concert with the D peak, as yet another sign of the extent of disorder.[26] These trends, plotted as the I_D/I_G and $I_{D'}/I_G$ ratios, are shown in Fig. 6a, while Fig. 6b illustrates the evolution in lattice strain as a function of time. After t = 87.5 min, it was observed that the laser position was shifting from the centre of the pore, and the spectral signal of the membrane was being conflated with that of the surrounding underlying carbon support matrix (not shown). Here, the laser was turned off, and the objective was realigned over the centre of the pore for data collection again at t = 112.5 min.

Taking these spectral data to be indicative of chemical reactions, in concert with estimates of the strain in the graphene from the Raman peak shifts, it is shown that for the first measurement of the strain in the graphene under applied force

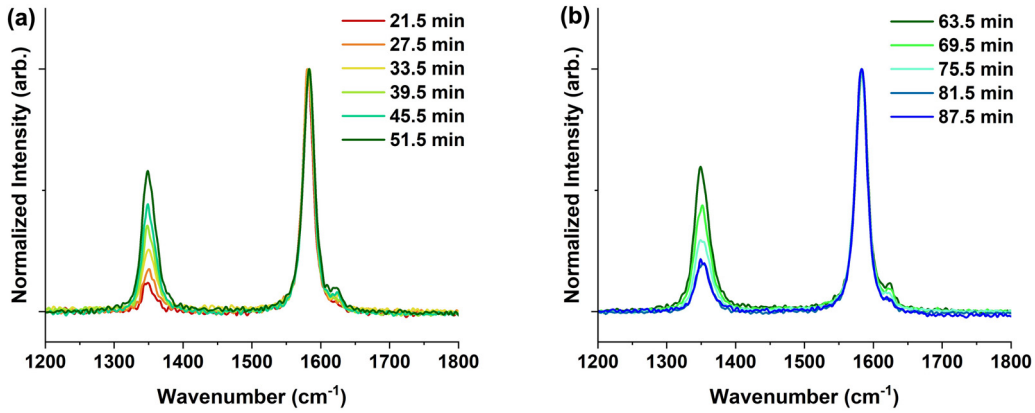

Fig. 5 Time-resolved spectra for suspended graphene under applied pressure from nanopure water. (a) Increasing I_D/I_G ratio as a function of time for the first half of the backing pressure experiment. (b) Decreasing I_D/I_G ratio as a function of time for the latter half of the backing pressure experiment. Select spectra are shown in 6-minute intervals for clarity. A full set of spectra can be found in the ESI† (Fig. S1).

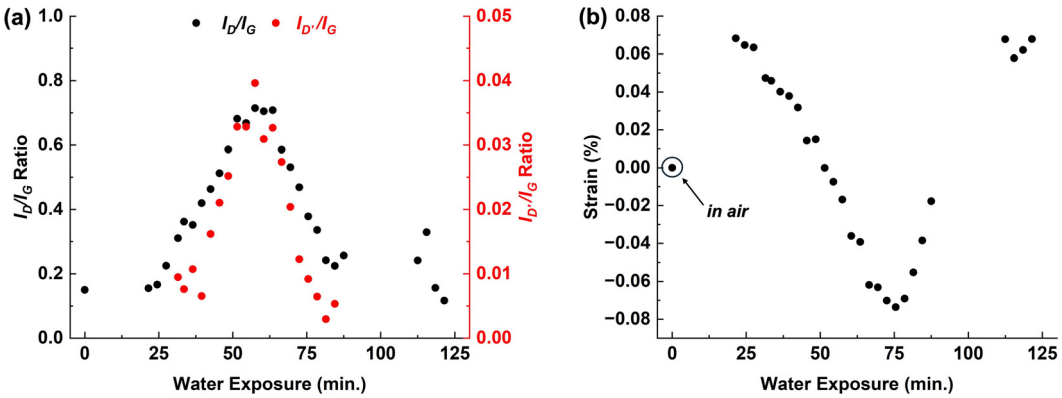

Fig. 6 Reactivity and strain of suspended graphene under applied pressure from nanopure water. (a) Change in I_D/I_G (black) and $I_{D'}/I_G$ (red) as a function of water exposure time. (b) Change in graphene lattice strain as a function of water exposure time.

at t = 21.5 min, we measure an areal strain 0.068% greater than the strain of the freestanding graphene in air. As reaction proceeds, and I_D/I_G increases, the strain starts to relax. As the graphene reacts and forms out-of-plane bonds, the local transition from sp^2 to sp^3 leads to a breaking of the surrounding π bonds, while the longer and more flexible in-plane σ bonds remain, decreasing the bond order. This decrease in bond order locally relaxes the areal strain that had built up as a response to the applied backing pressure of water.

It should be noted that the lattice strain continues to decrease even after the I_D/I_G ratio inverts (Fig. 6b). Thus, it does not seem that the decrease in the I_D/I_G ratio is a result of species desorbing from the lattice and returning the lattice to an ordered sp^2 character; rather, there is a continuation of out-of-plane bond formation that further alters the local structure of the graphene as described below.

To understand this transition, we turn to the work from Lucchese *et al.* which proposed a model to understand the evolution of the I_D/I_G ratio for graphitic species as a function of defect density.[34] From their model, whenever a point defect forms on the graphene surface, two types of changes occur to the local region. The immediate area of the defect is considered structurally disordered; this is the region where the lattice transition from sp^2 to sp^3 occurs. Surrounding each such region is an activated one which retains its sp^2 character. The proximity to the structurally disordered region, though, leads to the breaking of the Raman selection rules and the appearance of the D peak. Thus, the more the surface consists of activated regions, the larger the D peak will appear in a Raman spectrum. As more defects are introduced to the graphitic surface, progressively more of the surface is occupied by these structurally disordered and activated regions. However, as more out-of-plane bonds form, at a certain point the defect density crosses a critical threshold, and the structurally disordered regions grow at the expense of the activated regions. This relative decrease in these activated regions leads to a corresponding decrease in the I_D/I_G ratio. While Lucchese *et al.* developed this model using defects induced by Ar-ion bombardment,[34] the trend can be generalized to any point defects of the sp^2 lattice, such as the formation of covalent bonds. Numerically, the size of the structurally disordered and activated regions surrounding each defect will change based on the type of defect, but the trend holds.

One can calculate the distance between point defects before defect coalescence, L_D, based on the I_D/I_G ratio at the inflection point, by employing eqn (2),[34]

$$\frac{I_D}{I_G} = \frac{102}{L_D^2} \quad (2)$$

From the maximum I_D/I_G ratio in Fig. 6a, the L_D before defect coalescence was found to be ~11.8 nm. Additionally, the defect density can be calculated by the inverse of the square of the L_D. With L_D = 11.8 nm at the defect coalescence point, 0.007 bonds per nm^2 are formed. Assuming that the graphene unit cell has an area of 0.052 nm^2 given the C–C bond length of 1.42 Å,[35] then the C density in pristine graphene is 38.2 C atoms per nm^2. Thus, the maximum I_D/I_G ratio occurs when 0.02% of the sp^2 hybridized C atoms convert to sp^3. This corresponds qualitatively with work by Ferrari *et al.*,[36] which observed an increase in the I_D/I_G ratio of graphite with a negligible increase in sp^3 character indicative of a shift from uniform graphite to nanocrystalline graphite. This small value is not to be taken as a defect density *per se*, but as the percentage of C atoms that are now contributing to disruption of the crystalline network *via*, for example, grain boundaries. This was followed by a decrease in the I_D/I_G ratio as the extent of sp^3 character increased resulting from the nanocrystalline transition to amorphous carbon. In our case, we are likely seeing the transition from crystalline to nanocrystalline graphene with the initial I_D/I_G increase as bonding disrupts the lattice, followed by a transition to a more amorphous lattice with the resulting decrease in the I_D/I_G ratio. Future work will aim to carry-out transmission electron microscopy (TEM) measurements on the samples to attempt to image this transformation.[37–39] As our membrane samples are epoxied to the reactor caps however, we have no viable way of carrying out such studies without damaging the membrane at this time.

Eventually, the strain in the lattice starts to increase again, around t = 75.5 min (Fig. 6b). Over the duration of the experiment, water continued to apply a force against the lattice. While the lattice was initially able to relax through the breaking of the π bonds and the formation of out-of-plane bonds, it appears as if that was ultimately not enough to counter the applied force from the water, leading to the increase in strain present.

2.4 Computational analysis of the reaction of water with graphene

As the experimentally observed I_D/I_G trend relates to the functionalization and disorder of the graphene surface, density functional theory (DFT) was employed to elucidate atomic-scale processes that are accelerated when curvature is induced into the basal plane of graphene. Our theoretical model of water pressure inducing curved graphene only considers 1D curvature, as it was previously found that 1D and 2D curvature models provide similar information regarding the effect of curvature on reactivity.[17] The details for preparing curved graphene with compressive strain and overall computational settings are described in computational methods (Section 4.6). We analyse the reactivity of graphene *versus* the curvature of the graphene sheet, in addition to reactivity in the presence and absence of defects therein. Several chemical processes are possible on the graphene surface, including:

$$H_2O(g) + 2^* \rightleftharpoons H^* + OH^*$$

$$O_2(g) + 2^* \rightleftharpoons 2O^*$$

$$H_2O(g) + 2O^* \rightleftharpoons 2OH^* + O^*$$

where * indicates a surface site or a surface-bound species. As we focus on understanding the chemical processes qualitatively, solvent effects are not included.

We first study the curvature effect on water dissociation by calculating the reaction barrier on flat and curved pristine graphene (Fig. 7a). Though curvature stabilizes the transition state by 0.12 eV, the activation barrier is still too high (>3 eV) to trigger water dissociation on pristine flat or curved graphene. Accordingly, the curvature effect for water dissociation is investigated on graphene with defects. Epoxide defects are introduced as typical defects on the graphene surface because of the possibility of forming them *via* chemisorbed oxygen dissociation on carbon materials.[40,41] With the introduction of defects, the water dissociation barriers drop dramatically in energy (to below 1.5 eV) on both flat and curved graphene. For curved graphene with epoxide defects, the activation barrier is further decreased to 0.72 eV, making water splitting kinetically

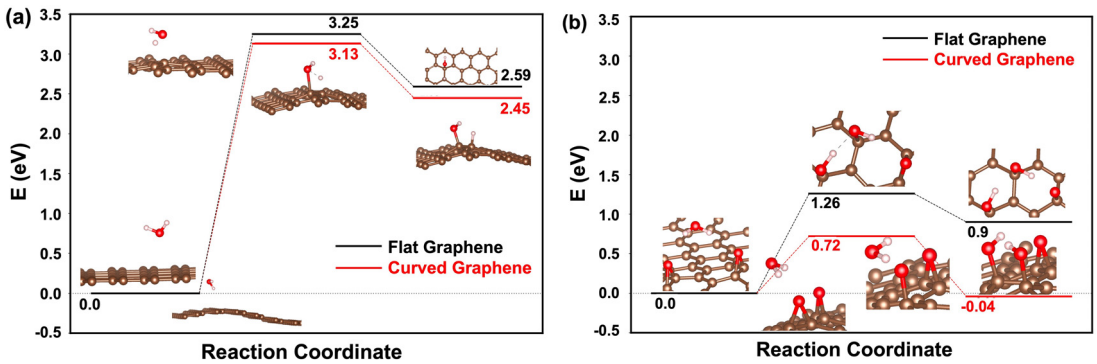

Fig. 7 (a) Reaction coordinate for the dissociation of water on pristine flat and curved graphene, which can be compared to (b) the reaction coordinate for the dissociation of water on flat and curved graphene with an adjacent epoxide defect.

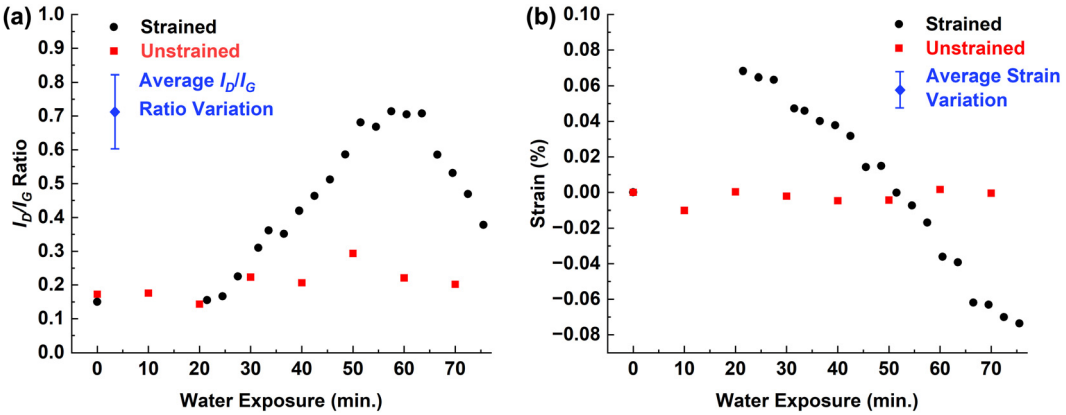

Fig. 8 Reactivity and strain of suspended graphene with and without an applied pressure. (a) Change in I_D/I_G for a membrane under pressure (black) and without pressure (red). (b) Change in graphene lattice areal strain as a function of water exposure. The blue scale bars shown in the legends correspond to the average deviations in measurements for the (a) I_D/I_G ratios (±0.09) and (b) the strain (±0.009%) across multiple point spectra, which can be considered the possible spread of deviation for any individual data point represented in the plots.

accessible (Fig. 7b). This indicates that defects are necessary to start the reaction. In addition, the comparison of defective graphene reactivity with and without curvature, the mechanical force which induces the curvature is also necessary to observe a significant reaction rate.

Other defects present on graphene – such as H* and OH* groups – were studied, and it was found computationally that adsorbed hydroxyl and hydrogen also accelerate the reaction under the effect of curvature, but that the epoxide defect is the dominant species to drive water dissociation (See ESI,† Table S1 and Fig. S2). Defects are required to initiate reaction, and the non-zero experimentally observed I_D/I_G values at t = 0 min suggest a finite initial population of functionalized carbon centres. The synergistic effects of defects and the curvature induced by mechanical force accelerate water dissociation and graphene functionalization, increasing the I_D/I_G ratio. As we have previously found that these defects preferentially concentrate near the mountain regions on curved graphene, water dissociation most likely occurs more feasibly at such sites,[17,22] because sp^3 formation is more likely to happen around the mountain sites of curved graphene. The unequal distribution of adsorbates and reaction sites leads to greater disordering of the graphene surface, breaking its periodicity, and driving it toward amorphous carbon as evidenced by the subsequent decrease in the I_D/I_G ratio. In the theoretical model, though defect coverage is higher than the observed defect density in experiments, we found that the activation barrier decreases slightly as the defect coverage is increased. The finding that the curvature of reaction can control graphene reactivity is sustained (See ESI,† Fig. S3). Overall, this aligns well with the experimental observations both in this and other works as discussed previously.

2.5 Comparison of reaction induced *via* applied pressure and simple exposure

It is apparent that there is a large increase in reactivity for strained membranes *versus* unstrained. Fig. 8 shows the comparisons of reactivity and strain for the graphene membrane reactions with and without backing pressure. The membrane without applied pressure had the same I_D/I_G ratio and the same strain for the duration of the experiment, within statistical error. While the average I_D/I_G ratio and strain did not change with increased exposure to water, there was some variation for individual pores.

The sample that was exposed to a backing pressure was clearly more reactive. A membrane exposed to a pressure high enough to induce an initial areal strain of 0.068% has a 5.0× increase in the I_D/I_G ratio *versus* its initial I_D/I_G ratio over air. With the application of pressure leading to out-of-plane distortion, there is an increased susceptibility to reaction *via* water exposure.

3. Conclusion

The changes in the spectral character of suspended graphene samples were monitored as a function of time. For samples that were exposed to water under ambient pressure, there was no change in average reactivity. When enough pressure was applied to a suspended sample to introduce a 0.068% increase in areal strain, there was a 5.0× increase in the I_D/I_G ratio with water exposure. Eventually an inflection point was reached where the I_D/I_G ratio decreased with further exposure, revealing defect coalescence when the bonded species are less than 11.8 nm apart on the lattice. This reaction is driven through the application of out-of-plane lattice distortion, as no change in the I_D/I_G ratio was seen for samples simply immersed in water. In concert with experiment, we theoretically modelled graphene reactivity with and without curvature and defects. We demonstrate that pristine graphene is unreactive to water, even in the presence of moderate curvature. We find that common stable defects, such as epoxides, dramatically catalyse water functionalization, especially for curved graphene. This model aligns with the experimentally found curvature-induced reactivity.

While here we have indirectly determined that there was out-of-plane membrane distortion through calculating the change in lattice strain, it would be beneficial to directly measure the pressure behind the membranes in the 2D-MSR. AFM will be

utilized to a greater extent in the future to further image membrane distortion in both this and other reactions. Additionally, forthcoming reactions will include modifications to the system to have a stronger quantitative measure of the backing pressure experienced by the membrane, while continuing to develop theoretical models of pressure- and curvature-induced graphene reactivity.

The reaction of graphene with water serves as a model system to elucidate fundamental information about mechanochemical processes. There remains much to uncover regarding the specifics of the tailorable applied forces in the 2D-MSR, but this reactor system will be helpful in advancing the capacity to explore 2D materials and their reactivities with a multitude of compounds under controllable pressure conditions. Uniting detailed mechanical and spectroscopic measurements with sophisticated electronic, elastic, and catalytic models will enable the design of intentionally functionalized nanomaterials and unprecedented mechanically tuneable nanocatalytic systems.

4. Experimental and computational methods

4.1 Materials

Samples were purchased from MSE Supplies (#ME0624) and consisted of a single layer of graphene that had previously been transferred *via* a wet transfer method onto a 12 nm amorphous carbon film over a 12 μm-thick Au electron microscopy (EM) grid. The amorphous carbon films contained square arrays of circular pores (2 μm in diameter; 6 μm pitch) which served as a periodic template of suspended and supported graphene. A silver-based two-part epoxy (EPOTEK H20E) was used for membrane adhesion.

4.2 2D-materials strain reactor (2D-MSR) specifications

The body of the reactor system is a 1″ wide stainless-steel rod that is ≈ 1.3″ long and has a wall thickness of 0.085″. The top 0.25″ of the rod has external threading to affix the caps which hold the membranes. The base of the rod was welded shut with a stainless-steel plate into which two holes, each 0.0625″ in diameter, were spaced 0.125″ apart. Each hole was welded to a bent 0.25″ stainless steel rod such that the opposite end of each rod was at a higher plane than the opening in the reactor body.

The reactor cell is made of polyetheretherketone. It is 0.83″ in diameter with a 0.25″ through-hole in the centre. A groove for a nitrile O-ring was cut into each face of the cell. This cell fits in the 1″ stainless-steel rod and is held in place by six evenly placed screws about the exterior circumference such that the 110 O-ring on the internal face of the reactor is compressed tightly against the stainless-steel plate. When the Al caps are threaded into place, the 112 O-ring on the external face of the reactor is compressed against the cap.

The custom-made Al caps contain a 3 mm wide, 200 μm deep inset groove and 1″ wide internal threads. A 1 mm through-hole in the cap underneath the membrane allows for direct contact between the lattice of the graphene with the applied liquid or gas in the reactor. This hole aligns with the reactor's 0.25″ through-hole. The 2D-MSR is affixed to a square 4 × 4″ plate that was fabricated for a WITec Alpha 300 RA confocal microscope, such that the 2D-MSR could sit level on the plate. The tubing which allows for the flow of liquids or gases into and out of the 2D-MSR is 0.25″ diameter polyvinyl chloride (PVC) tubing. Swagelok male-to-male fittings of the same diameter were used to connect to the 2D-MSR's inlet and outlet rods.

4.3 Transfer of membranes onto Al caps

Samples were adhered to the centre of the Al caps described above. The hole was previously bored through the centre of the cap so that, when the membrane is adhered, the bottom side can be in contact with a liquid or gas flowing through the reactor. A thorough mixture of 1 : 1 w/w of silver epoxy was applied to the inset of the cap, to which the membrane was carefully placed level to the top of the cap. A small amount of adhesive was added to the rim of the cap to prevent leakage. The membrane was cured by placing on a hot plate in a laminar flow hood at 80 °C. The temperature was increased by 10 °C every 5 min before holding at 150 °C for 1 h. The caps were allowed to cool to room temperature and stored in a desiccator.

4.4 Operation of 2D-MSR

The system is a series of components connected *via* PVC tubing whose key feature is the 2D-MSR reactor core. In this case, water flows through the tubing and into the reactor, though the tubing can be changed if there are solvent compatibility issues. A peristaltic pump draws the water from a storage receptacle into the tubing and facilitates its flow through the circuit. Before reaching the 2D-MSR, the water traverses a pressure gauge which can be monitored over the course of a given experiment. The liquid then enters and subsequently exits the 2D-MSR after passing through the reactor.

While flowing through the 2D-MSR, the liquid presses against the membrane on the top of the reactor. The final component of the circuit is a fine-needle pressure valve which can be adjusted to modify the amount of backing pressure experienced by the membrane at the membrane-liquid interface. The flow rate was approximately 3 mL min^{-1}, and it took just over eleven minutes for the entire circuit to be filled with water. The travel time from the inlet to the outlet of the reactor generally varies between 90 and 150 seconds at this flow rate.

4.5 Reaction monitoring

4.5.1 Raman spectroscopy. A WITec Alpha 300RA confocal microscope equipped with a 488 nm diode laser, a UHTS 300 VIS spectrometer, and a cooled (−60 °C) Andor EMCCD detector was used for all Raman measurements. The laser intensity was measured to be < 150 μW at the 100× objective (Nikon E Plan, 0.9 NA). Laser intensities higher than this led to warping of the amorphous carbon matrix. Before collecting measurements, the Al caps with adhered membranes were placed on the *in situ* 2D-MSR reactor system as described above. For all spectral measurements, a 600 g mm^{-1} grating was used (resolution < 3 cm^{-1}). All point

spectra are the average of 20 individual consecutive spectra, each with a 3 s integration time. Spectra were background subtracted and Lorentz fits were applied to the D, G, and 2D peaks for each using OriginPro 2021.

4.5.2 Reaction without backing pressure. Membranes adhered to Al caps were exposed to nanopure water (pH 7) in 10 min intervals for a cumulative exposure time of 70 min. The caps were inverted and propped up on the edges of the face of the cap before 1 mL of water was deposited into the thread-side, allowing the bottom of the membrane to be in contact with the water. After each 10 min increment, the water was removed with a disposable pipette and the cap was placed thread-side down on a hot plate at 80 °C for 5 min to remove residual water. Samples were attached to the 2D-MSR and Raman measurements were taken of 5 individual pores.

4.5.3 Reaction with backing pressure. Membranes adhered to Al caps were attached to the 2D-MSR and nanopure water (pH 7) was allowed to flow through the system at a rate of $\approx$ 3 mL min^{-1} by connection to a peristaltic pump. Raman spectra were taken in three-minute increments.

4.6 Computational and theoretical approach

The QUANTUM ESPRESSO software package has been used to perform density functional theory calculations.[42] The kinetic barriers for adsorbate migrations are calculated using the climbing image nudged elastic band method.[43] A (6 × 6) supercell of graphene has been used to understand the effect of curvature on the migration barrier. We have inserted a vacuum layer (*ca.* 20 Å) between the graphene planes in the simulation. A Γ centred (3 × 3 × 1) *k*-point grid is implemented to sample the Brillouin zone. Electronic exchange–correlation energy was calculated using the generalized gradient approximation.[44] OPIUM (version 3.7) software is used to generate designed, optimized, norm-conserving, and non-local pseudopotentials.[45–47] The energy cut-off used was 50 Ry to expand the wave functions of the valence electrons in a plane wave basis. Further, we used DFT-D3 dispersion correction to capture the dispersion and non-covalent interactions to include van der Waals effects when modelling curved graphene.[48] One-dimensional curvature (cylindrical distortion) is induced along one direction to achieve the 0.2 nm^{-1} radius of curvature, corresponding to 5 nm radius of a nanoparticle, which can represent the graphene structure under the out-of-plane distortions in experiments.[48] In a recent work,[23] we demonstrated that one-dimensional (cylindrical) and two-dimensional (hemispherical) curvature offer similar enhancements to the chemical reactivity of graphene.

Author contributions

Conceptualization and experimental methodology by NH and JDB. Exposure and pressurized experiments performed by NH with assistance from JH and CC. Data analysis by NH and EJB. Validation of experimental results by EJB and UDB. Theoretical framework by YB, SB, and AMR. Computational work by YB and QM. Written by NH with assistance from EJB, YB, QM, AMR, and JDB. Reviewed and edited collaboratively. Project administrated and supervised by AMR and JDB. All authors have given approval to the final version of the manuscript.

Data availability

Data for this communication are available through Figshare at **https://doi.org/10.6084/m9.figshare.26765020**.

Conflicts of interest

There are no conflicts of interest for this work.

Acknowledgements

This work was supported by the NSF Center for the Mechanical Control of Chemistry under Grant # CHE-2023644 and # CHE-2303044. SB acknowledges the Vagelos Institute for Energy Science and Technology for a graduate fellowship.

References

1 T. Friščić, C. Mottillo and H. M. Titi, *Angew. Chem., Int. Ed.*, 2020, **59**, 1018–1029.
2 X. Liu, Y. Li, L. Zeng, X. Li, N. Chen, S. Bai, H. He, Q. Wang and C. Zhang, *Adv. Mater.*, 2022, 2108327.
3 K. J. Ardila-Fierro and J. G. Hernández, *ChemSusChem*, 2021, **14**, 2145–2162.
4 P. Lavalle, F. Boulmedais, P. Schaaf and L. Jierry, *Langmuir*, 2016, **32**, 7265–7276.
5 O. Azzaroni, B. Trappmann, P. van Rijn, F. Zhou, B. Kong and W. T. S. Huck, *Angew. Chem., Int. Ed.*, 2006, **45**, 7440–7443.
6 A. A. L. Michalchuk, E. V. Boldyreva, A. M. Belenguer, F. Emmerling and V. V. Boldyrev, *Front. Chem.*, 2021, **9**, 685789.
7 H. Carlton, D. Huitink and H. Liang, *Lubricants*, 2020, **8**, 87.
8 K. i Hiratsuka and C. Kajdas, *Proc. Inst. Mech. Eng., Part J*, 2013, **227**, 1191–1203.
9 F. Chemat, M. Abert Vian, A.-S. Fabiano-Tixier, M. Nutrizio, A. Režek Jambrak, P. E. S. Munekata, J. M. Lorenzo, F. J. Barba, A. Binello and G. Cravotto, *Green Chem.*, 2020, **22**, 2325–2353.
10 K. Wu, T. Ju, Y. Deng and J. Xi, *Trends Food Sci. Technol.*, 2017, **66**, 166–175.
11 X. Zhao, Y. Wei, Z. Wang, B. Zhang, F. Chen and P. Zhang, *J. Food Sci.*, 2011, **76**, R134–R142.
12 S. Mateti, M. Mathesh, Z. Liu, T. Tao, T. Ramireddy, A. M. Glushenkov, W. Yang and Y. I. Chen, *Chem. Commun.*, 2021, **57**, 1080–1092.
13 E. Gil-González, M. d R. Rodríguez-Laguna, P. E. Sánchez-Jiménez, A. Perejón and L. A. Pérez-Maqueda, *J. Alloys Compd.*, 2021, **866**, 158925.
14 E. Nwoye, S. Raghuraman, M. Costales, J. Batteas and J. R. Felts, *Phys. Chem. Chem. Phys.*, 2023, **25**, 29088–29097.
15 W. Yuan, Y. Zhou, Y. Li, C. Li, H. Peng, J. Zhang, Z. Liu, L. Dai and G. Shi, *Sci. Rep.*, 2013, **3**, 2248.

16 Y. Ouyang, C. Ling, Q. Chen, Z. Wang, L. Shi and J. Wang, *Chem. Mater.*, 2016, **28**, 4390–4396.
17 N. Hawthorne, S. Banerjee, Q. Moore, A. M. Rappe and J. D. Batteas, *J. Phys. Chem. C*, 2022, **126**, 17569–17578.
18 Q. Wu, Y. Wu, Y. Hao, J. Geng, M. Charlton, S. Chen, Y. Ren, H. L. Hengxing Ji, D. W. Boukhvalov, R. D. Piner, C. W. Bielawski and R. S. Ruoff, *Chem. Commun.*, 2013, **49**, 677–679.
19 Y. Qu, Y. Ke, Y. Shao, W. Chen, C. T. Kwok, X. Shi and H. Pan, *J. Phys. Chem. C*, 2018, **122**, 25331–25338.
20 Y. Zhang, Q. Fu, Y. Cui, R. Mu, L. Jin and X. Bao, *Phys. Chem. Chem. Phys.*, 2013, **15**, 19042–19048.
21 D. W. Boukhvalov and M. I. Katsnelson, *J. Phys. Chem. C*, 2009, **113**, 14176–14178.
22 S. Banerjee and A. M. Rappe, *ACS Mater. Lett.*, 2023, **5**, 574–579.
23 S. Banerjee, N. Hawthorne, J. D. Batteas and A. M. Rappe, *J. Am. Chem. Soc.*, 2023, **45**, 26765–26773.
24 S. Banerjee and A. M. Rappe, *J. Am. Chem. Soc.*, 2022, **144**, 7181–7188.
25 M. A. Pimenta, G. Dresselhaus, M. S. Dresselhaus, L. G. Cançado, A. Jorio and R. Saito, *Phys. Chem. Chem. Phys.*, 2007, **9**, 1276–1290.
26 M. S. Dresselhaus, A. Jorio, A. G. Souza Filho and R. Saito, *Philos. Trans. R. Soc., A*, 2010, **368**, 5355–5377.
27 Y. Yao, W. I. Shin, H. Chen, S.-M. Lee, S. Manickam, S. Hanson, H. Zhao, E. Lester, T. Wu and C. H. Pang, *Carbon Lett.*, 2021, **31**, 177–199.
28 M. Hou, W. Cen, F. Nan, J. Li and Y. Chu, *RSC Adv.*, 2016, **6**, 7015–7021.
29 M. K. Kostov, E. E. Santiso, A. M. George, K. E. Gubbins and M. B. Nardelli, *Phys. Rev. Lett.*, 2005, **95**, 136105.
30 R. S. Weatherup, B. Eren, Y. Hao, H. Bluhm and M. B. Salmeron, *J. Phys. Chem. Lett.*, 2016, **7**, 1622–1627.
31 Y.-H. Lu, J. M. Larson, A. Baskin, X. Zhao, P. D. Ashby, D. Prendergast, H. A. Bechtel, R. Kostecki and M. Salmeron, *Nano Lett.*, 2019, **19**, 5388–5393.
32 J. E. Lee, G. Ahn, J. Shim, Y. S. Lee and S. Ryu, *Nat. Commun.*, 2012, **3**, 1024.
33 Y. Zhang, M. Heiranian, B. Janicek, Z. Budrikis, S. Zapperi, P. Y. Huang, H. T. Johnson, N. R. Aluru, J. W. Lyding and N. Mason, *Nano Lett.*, 2018, **18**, 2098–2104.
34 M. M. Lucchese, F. Stavale, E. H. M. Ferreira, C. Vilani, M. V. O. Moutinho, R. B. Capaz, C. A. Achete and A. Jorio, *Carbon*, 2010, **48**, 1592–1597.
35 L. P. Biró, P. Nemes-Incze and P. Lambin, *Nanoscale*, 2012, **4**, 1824–1839.
36 A. C. Ferrari and J. Robertson, *Phys. Rev. B: Condens. Matter Mater. Phys.*, 2000, **61**, 14095–14107.
37 P. Y. Huang, C. S. Ruiz-Vargas, A. M. V. D. Zande, W. S. Whitney, M. P. Levendorf, J. W. Kevek, S. Garg, J. S. Alden, C. J. Hustedt, Y. Zhu, J. Park, P. L. McEuen and D. A. Muller, *Nature*, 2011, **469**, 389–392.
38 J. C. Meyer, C. Kisielowski, R. Ernie, M. D. Rossell, M. F. Crommie and A. Zettl, *Nano Lett.*, 2008, **8**, 3582–3586.
39 J. C. Meyer, A. K. Geim, M. I. Katsnelson, K. S. Novoselov, T. J. Booth and S. Roth, *Nature*, 2007, **446**, 60–63.
40 F. Mehmood, R. Pachter, W. Lu and J. J. Boeckl, *J. Phys. Chem. C*, 2013, **117**, 10366–10374.
41 R. T. Yang and C. Wong, *J. Chem. Phys.*, 1981, **75**, 4471–4476.
42 P. Giannozzi, S. Baroni, N. Bonini, M. Calandra, R. Car, C. Cavazzoni, D. Ceresoli, G. L. Chiarotti, M. Cococcioni and I. Dabo, *J. Phys.: Condens. Matter*, 2009, **21**, 395502.
43 G. Henkelman, B. P. Uberuaga and H. Jónsson, *J. Chem. Phys.*, 2000, **113**, 9901–9904.
44 J. P. Perdew, K. Burke and M. Ernzerhof, *Phys. Rev. Lett.*, 1996, **77**, 3865–3868.
45 J. Yang, *Opium - pseudopotential generation project*, **https://opium.sourceforge.net/index.html**, (accessed 14 September, 2021).
46 N. J. Ramer and A. M. Rappe, *Phys. Rev. B: Condens. Matter Mater. Phys.*, 1999, **59**, 12471–12478.
47 A. M. Rappe, K. M. Rabe, E. Kaxiras and J. D. Joannopoulos, *Phys. Rev. B: Condens. Matter Mater. Phys.*, 1990, **41**, 1227–1230.
48 S. Grimme, J. Antony, S. Ehrlich and H. Krieg, *J. Chem. Phys.*, 2010, **132**, 154104.

